Optimizing Deep-stall Landing Maneuvers on Small Fixed-wing UAVs

ETH
Eidgenössische Technische Hochschule Zürich
Swiss Federal Institute of Technology Zurich

Autonomous Systems Lab
Prof. Roland Siegwart

Semester Thesis

Optimizing Deep-stall Landing Maneuvers on Small Fixed-wing UAVs

Spring Term 2019

Supervised by:
Thomas Stastny
Nick Lawrance

Author:
Gian-Andrea Heinrich

Eidgenössische Technische Hochschule Zürich
Swiss Federal Institute of Technology Zurich

Declaration of originality

The signed declaration of originality is a component of every semester paper, Bachelor's thesis, Master's thesis and any other degree paper undertaken during the course of studies, including the respective electronic versions.

Lecturers may also require a declaration of originality for other written papers compiled for their courses.

I hereby confirm that I am the sole author of the written work here enclosed and that I have compiled it in my own words. Parts excepted are corrections of form and content by the supervisor.

Title of work (in block letters):

Authored by (in block letters):
For papers written by groups the names of all authors are required.

Name(s):	**First name(s):**

With my signature I confirm that

- I have committed none of the forms of plagiarism described in the 'Citation etiquette' information sheet.
- I have documented all methods, data and processes truthfully.
- I have not manipulated any data.
- I have mentioned all persons who were significant facilitators of the work.

I am aware that the work may be screened electronically for plagiarism.

Place, date	**Signature(s)**

For papers written by groups the names of all authors are required. Their signatures collectively guarantee the entire content of the written paper.

Contents

Preface

This project report has been written in the course of the compulsory semester project in the third semester of my masters in mechanical engineering at ETH Zurich in the spring semester 2019.

I owe my deepest gratitude to Thomas Stastny and Nicholas Lawrance for their support. As my supervisors, they guided and assisted me through this project. I could approach them whenever answers or advice was needed.
Further, I want to thank the staff of the ASL who supported me whenever they could.
I want to express my thankfulness towards Professor Roland Siegwart, who oversaw this work and made it possible.

Last but not least I want to express my gratitude to all people not mentioned by name, whose help I have encountered during my semester thesis.

Thank you!

Abstract

The increasing importance of UAVs in today's world is undisputed. However, fixed-wing UAVs are often marginalized. This marginalization is often caused by the difficulties landing them. Landing in deep-stall is an approach to deal with this issue. It allows landing at steep flightpath angles and at low horizontal speed, thanks to massively increased drag and reduced lift. This is possible without needing any additional tools like parachutes or nets. Furthermore, the range does not get reduced as it would by using VTOL planes. This work focuses on developing a simple and durable fixed-wing development platform which allows investigating the influence of thrust on the sink rate during deep-stall maneuvers. In addition, it can help to improve the understanding of deep-stall over a wider set of input parameters allowing the achievement of a variety of different flightpath angles as well as better characterization of deep-stall for small UAVs. The developed airframe is able to enter and maintain deep-stall automatically and to do partially manual control deep-stall landings. A feasible space of possible input parameters has been defined. Additionally, a second order utility function has been derived. Finally, a control approach is proposed which allows control of the sink rate in a computationally inexpensive way.

Symbols

Symbols

θ	Pitch angle
γ	Flightpath angle
α	Angle of attack
ρ	Air density
L	Lift force
D	Drag force
C_L	Lift coefficient
C_D	Drag coefficient

Acronyms and Abbreviations

COTS	Commercial Of The Shelf
PWM	Pulse Width Modulation
AGL	Above Ground Level
COG	Center Of Gravity
CFD	Computational Fluid Dynamics
UAV	Unmanned Aerial Vehicle
ASL	Autonomous Systems Lab
ETH	Swiss Federal Institute of Technology

Chapter 1

Introduction

The abilities and distribution of small UAVs increased dramatically over the last decade[1]. There is a wide field of applications for small UAVs. It ranges from search and rescue over reconnaissance to mapping and delivery. Especially multi-copter were able to grab a large piece of the market due to their high maneuvrability and ease of operation. Even though, fixed-wing UAVs have a much longer range and higher flight speed combined with a larger payload capability, they are not that popular yet [2]. Their main disadvantage is their need for a landing field or other, mostly complicated, landing techniques. Especially in remote areas like mountain ranges, forests or at sea, where the long range and the higher speed of a fixed wing UAV would provide a lot of possibilities, it remains challenging to find suitably-large landing sites free from obstructions. There are already a few different recovery approaches to land without major space requirements, like net-recovery and parachute landing [3]. Parachute landings have several disadvantages. They are sensitive to wind and result in substantial extra effort to pack the parachute, not to mention the additional weight of the parachute, thereby reducing the range and the payload of the plane. Net-recovery on the other hand implies a large hassle to build up and transport all the necessary equipment and also causes large forces on the airframe during the net landing [3]. First proposed by Crowther and Prassas [4] in the year 2000, deep-stall landing for UAV research underwent a renaissance over the last few years. The advances in light flight controllers like the Pixhawk were most likely the key drivers.

There are several papers which have shown the theoretical feasibility of deep-stall recovery. Cheng and Guo [3] used a six degree of freedom CFD simulation to show the influence of different COG and elevator angles on deep-stall trajectories. Mathisen et al. [5] developed a non-linear model predictive controller to enable high precision deep-stall landing. They verified their result using a simulation. Further, they identified two main challenges. At low speeds, the control surfaces lose significantly in effectiveness and due to the increased drag in deep-stall flight conditions a massive decrease in wind disturbance rejection performance has to be expected. He et al. [2] investigated the influence of morphing parts, like a moving aerodynamic center on deep-stall approaches using a simulation. They could show theoretically that precise deep-stall landings are possible.

An airplane in a stalled condition is a highly non linear system and hard to predict as well as to simulate. Thus it is essential to interpret simulations carefully and rely on experimental data as well. Taniguchi [6] used a trim analysis to show that a stable trim condition exists in a deep-stall configuration. Additionally, a MATLAB/ Simulink simulation was used to compute certain trajectories. Finally they tried to

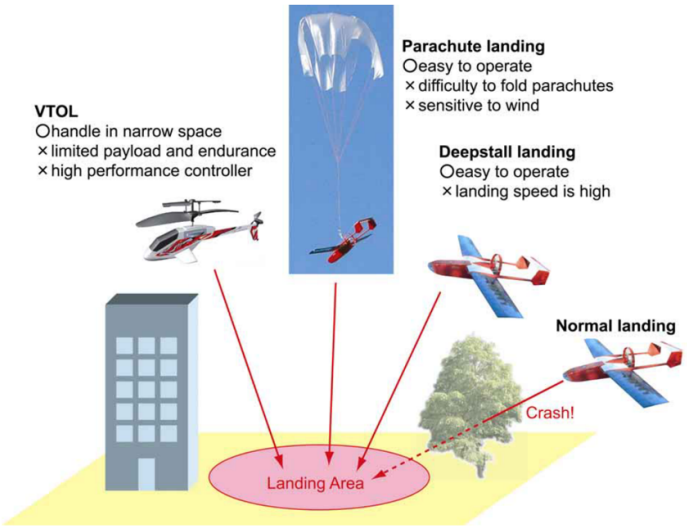

Figure 1.1: Advantages and disadvantages of different approach techniques. [6]

verify the results using a demonstrator plane. Thomas et al. [1] examined different approach techniques like butterfly, spin, deep-stall and thrust vectoring. The main challenges and possible air plane configurations were shown. Lately, perching got a more important role. It is a bionic concept which is inspired by birds. A large disadvantage of this concept is the needed undershoot to land. Waldock et al. [7] used a highly morphing plane and deep reinforcement learning to reduce the undershoot significantly.

There are already a few UAV capable of deep-stall landing available. For example the Aerovironment Pointer is capable to do so [8]. However, they are not using the motor to control the sink rate and thus, a thick plating or in case of the Pointer a disassembly on impact is necessary.

This work aims to develop a simple research platform having the size of a small UAV which can be used to gather deep-stall flight data autonomously. This data can be used to map different sink rates and forward velocities to distinct air craft states which can be used to implement a controller allowing precision landings with a steep approach path. Further, this data should help to increase the in-depth understanding of small UAV flying in deep-stall conditions.

There are three main sections. In section 3 the research platform is explained. In section 4 the experiment and the methodology is explained. After that, the findings are discussed and analysed in section 5. Additionally, a possible control approach is introduced. In section 6, a conclusion sums up the main results and a brief outlook indicates improvements and possible further steps.

Chapter 2

Deep-stall Fundamentals in Theory and Practice

2.1 Deep-Stall

Deep-stall is mainly known as an extreme dangerous stall state, especially for T-tail planes. At high angle of attack, the turbulent air caused by the main wing enfolds the horizontal stabilizer and renders it useless (Figure: 2.1). Depending on the airframe it reaches a stable state and is not recoverable. There are several major incidents reported where passenger planes got locked in this stable stall state and couldn't recover any more. Thus, it is also known as "locked in stall", "stable stall" or "super stall" [9, 10]. NASA investigated this phenomenon intensively during the the 1960-1990 time period. NASA research covered a broad range from simulator studies [11, 12], wind tunnel research [13] and flight testing [14, 15].
In figure 2.3 it is shown that there are three trim points. Usually, just the first one is used during normal flight. In deep-stall, the third one can be used as well. In opposite to the other two, the second one is unstable and occurs during the transition phase.

2.2 Deep-Stall approach procedures

In stall, the drag of an airplane gets increased significantly. On the other hand, the lift gets reduced. This allows to lose altitude relatively fast and in a controlled fashion with a steep approach angle. The increased drag reduces the vertical and horizontal velocity. Using a tractor propeller, the propwash can be used to reduce the vertical speed even further. To exploit deep-stall for UAV, it is essential not to aim for the uncontrolled flight state as mentioned in the last paragraph. To obtain

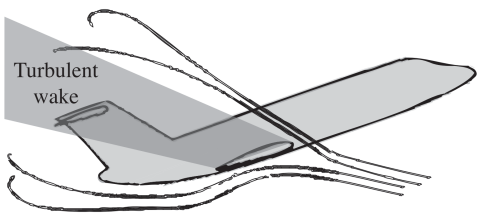

Figure 2.1: a) T-tail plane in deep-stall, the horizontal stabilizer is in turbulent air and loses significantly in authority. [1]

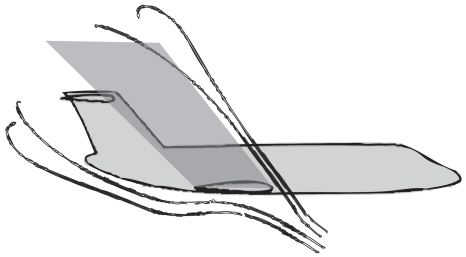

Figure 2.2: b) T-tail plane in post deep-stall, it's horizontal stabilizer is not in turbulent air and can be used to control the air plane. [1]

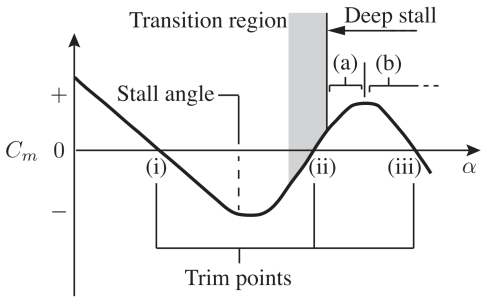

Figure 2.3: There are three trim points in this plot. The first one corresponds to a stable one during normal flight. The second one is an unstable trim point during stall and the last one is again stable and can be achieved in deep-stall.[6]

a stable deep-stall without complete loss of elevator authority, it is important to maintain a flow over the horizontal stabilizer and avoid stalling the stabilizer surfaces. This can be achieved by keeping it out of the turbulent flow caused by the stalled main wing (Figure: 2.2) and by using an all moving tail to stay in the attached airflow. To obtain a consistent and stable trajectory, the pitching moments need to be balanced. This can be achieved, after a critical angle of attack has been reached. In this state, the drag and lift force can be stabilized as well [1]. Figure 2.4 shows the force equilibrium during a deep-stall approach. The lift (L) and drag (D) forces cancel out the gravitational force. The lift induced from the horizontal stabilizer (L_h) cancels out any moments. Following angles are introduced to better describe the flightpath and the plane's attitude. θ is the pitch angle and corresponds to the vertical orientation of the body of the inertial coordinate system. The flightpath angle is indicated by γ and is defined as the angle between the horizontal plane and the plane's airspeed vector. α is better known as angle of attack and describes the difference between the plane's attitude and the flightpath. Usually, this equilibrium is found at high angles of attack and high flightpath angles. Thus, the pitch angle is small. This is crucial for a successful deep-stall landing. Otherwise, the plane wouldn't land on its belly and the load on its tail would be too large.

Figure 4.3 explains the different phases of a deep-stall approach procedure. First, the plane is in a normal flight state. In a second step, it turns into the wind to exploit the steepest possible approach path (in the inertial frame) and improve the stability during the approach and the transition phase. To enter deep-stall, the plane needs to pitch up and to exceed the stalling angle of attack. After a short unstable period, the plane reaches a post stall angle of attack and an equilibrium can be established. This stable state is maintainable until the plane lands or the plane recovers and flares out conventionally.

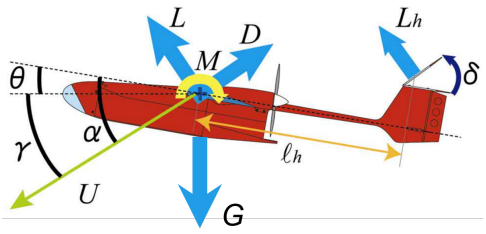

Figure 2.4: The forces which act on a plane during deep-stall to counter act the gravity. A stable equilibrium can be achieved.[6]

2.3 Lift and Drag Coefficient

Lift and drag as well as their coefficients play an important role in obtaining an in-depth understanding of the deep-stall maneuvres. Thus, a few important formulae and concepts are introduced in the next few paragraphs. According to Wildi [16], these are the general equation of motion of a soaring-plane in the vertical plane.

$$D - mgsin(\gamma) = m\dot{V} \tag{2.1}$$

$$L - mgcos(\gamma) = mV\dot{\gamma} \tag{2.2}$$

Equation 2.1 describes the equation of motion in x direction, where x is the direction of flight. Equation 2.2 gives the equation of motion in z direction with z being perpendicular to the direction of flight of the airplane.
The steady state lift and drag coefficients can be obtained by using the following two formulae and the lift and drag forces from the equations 2.1 and 2.2 [16, 17].

$$C_L = \frac{2 * L}{\rho * V^2 * A_{Wing}} \tag{2.3}$$

$$C_D = \frac{2 * D}{\rho * V^2 * A_{Wing}} \tag{2.4}$$

Studies like Pointer et al. [18] assume the aircraft to be a flat plate and use equation 2.5 to compute the lift coefficient and equation 2.6 or slightly adapted versions to compute the drag coefficient in the post-stall region [19, 20].

$$C_L = 2\pi sin(2\alpha) \tag{2.5}$$

$$C_D = 2sin(\alpha)^2 \tag{2.6}$$

For regular flight conditions, the following simplified formulas can be used. [18]

$$C_L = C_{L_0} + C_{L_\alpha}\alpha \tag{2.7}$$

$$C_D = C_{D_0} + KC_L^2(\alpha) \tag{2.8}$$

Using a distribution function allows to combine both regimes to one.

$$\begin{aligned} f_{combined} &= f * f_{dist} + f * (1 - f_{dist}) \\ f_{dist} &= \frac{1}{2} + \frac{1}{2} * cos(\pi * constrain(\frac{\alpha - (\alpha_{cut} - \frac{1}{2}\Delta\alpha)}{\Delta\alpha}), 0, 1)) \end{aligned} \tag{2.9}$$

Table 2.1: Explanation of the less common parameters.

Parameter	Meaning
A_{Wing}	Wing area
K	Scaling parameter
V	Airspeed
α_{cut}	Angle of attack where the flow regimes change
$\Delta\alpha$	Width of the transition region

2.4 Induced Rotational Moments

Most single engine planes have propellers rotating clockwise. Therefore, planes with a tractor propeller are exposed to major swerve to the left effects at high thrust, slow flight and high angles of attack. In this state, the aerodynamic forces are low and the propeller induces higher forces than usual. Four effects are identified as the major causes [21].

Torque: The propeller is rotating clockwise and thus inducing a counter clockwise moment on the plane. There are design features like specially angled aerodynamic surfaces or tilted motor mounts, which counter act the aforementioned effect in cruise flight. At low speeds, and high thrust those features are rendered useless or lose influence massively [21]. (Figure: 2.5)

Spiraling slipstream: The propeller causes a rotating airflow around the aircraft. This changes the airflow at the vertical stabilizer. The direction of the propeller lets the vertical stabilizer been hit from the left causing a yaw moment to the left [21]. (Figure: 2.6)

Gyroscopic precession: The gyroscopic precession is the only effect which can act in both directions. A change in pitch induces a force ether to the left or the right, causing a corresponding yaw effect [21]. (Figure: 2.7)

Asymmetrical thrust: If a plane is flying at high angles of attack, the angles of attack of the propeller blade differ. The ascending blade has a much lower angle of attack than the descending. This causes an asymmetric thrust. It is also know as the p-factor. The plane experiences a left pointing yaw moment [21]. (Figure: 2.8)

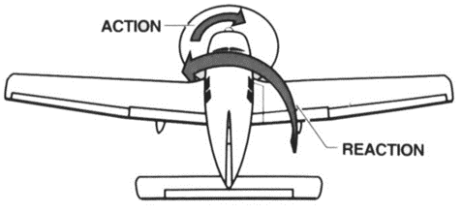

Figure 2.5: The propeller induces a torque moment on the aircraft [21].

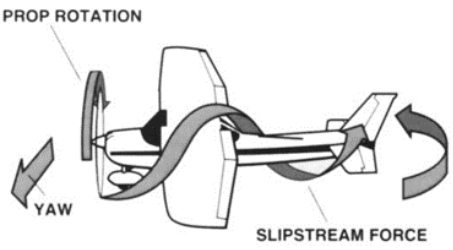

Figure 2.6: Spiraling slipstream wraps around the airplane and strikes the left side of vertical stabilizer causing a yaw to the left effect [21].

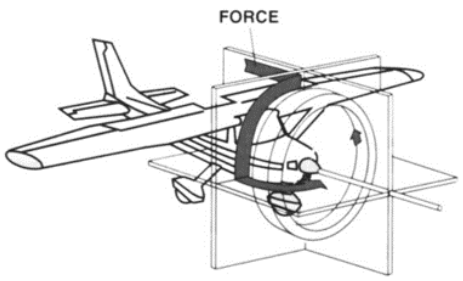

Figure 2.7: The propeller acts like a gyroscope. Depending on pitch changes a force is induced to the left or the right resulting in a yaw effect [21].

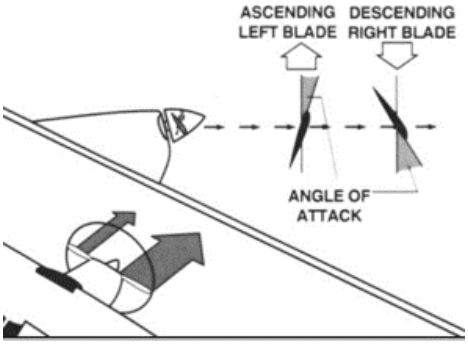

Figure 2.8: At high plane angle of attack, the ascending blade has a smaller propeller angle of attack than the descending one. Thus, an uneven and asymmetrical thrust is produced. The aforementioned effect is better known as the P-factor and causes the plane to yaw to the left [21].

Chapter 3

Research Platform

The research platform has to be durable, simple, deep-stall capable and easily available. Thus, a COTS RC plane has been chosen. Obviously, a few modifications are necessary.

3.1 Airframe

The chosen RC-plane is an EasyGlider from Multiplex. This plane is relatively inexpensive, easily available and durable. A further advantage is its conventional tail design. A T-tail could lead to an unrecoverable stall configuration and a V-tail makes a modification to an all moving tail much harder. Another advantage is the quite spacious fuselage. Thus, it is possible to fit in the flight controller and fairly large batteries. The Easy Glider has the dimensions of a typical small UAV. It has a wingspan of approx. 1800 mm and a stock take off weight of approx. 1100g. The modified version (Figure 3.1) has a take of weight of approx. 1400g. The thrust to weight ratio is significantly smaller than one. Otherwise, a tail sitting VTOL approach would be possible. The tractor propeller allows to investigate the influence of the prop-wash on the wing and thus on the sink rate.

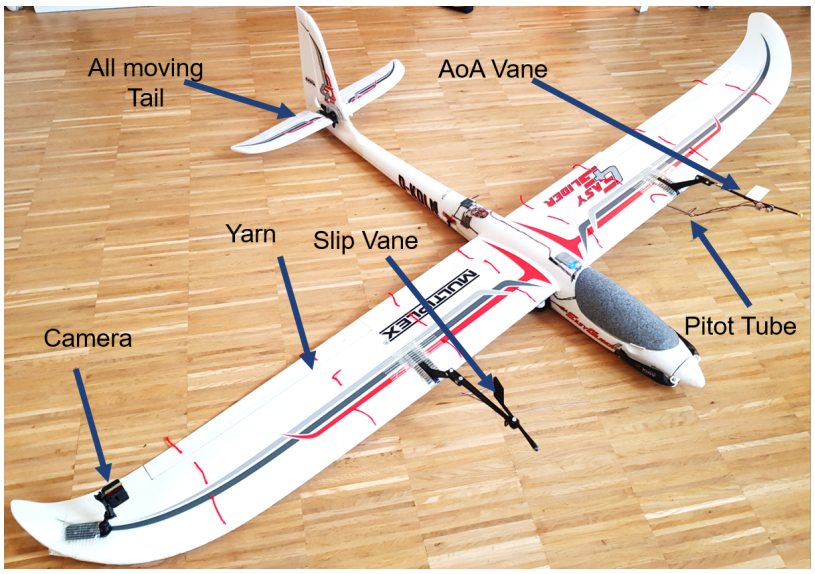

Figure 3.1: This figure shows an overview over the final research platform. Remarkable are the all-moving tail, the vanes, the moved servos and the camera position.

3.2 Modifications

Since it is not possible to enter and maintain deep-stall with a stock EasyGlider due to insufficient elevator control authority, it was obvious that modifications were necessary. Several previous papers showed the need of either larger elevator or complete all moving tails for small UAVs [1, 6] or normal planes [14, 15]. Thus, an all moving tail was added (Figure 3.2). It allows elevator deflections up to 52°. With this, it was already possible to fly deep-stall maneuvres. Therefore, further proposed modifications like a larger rudder, flaps and all moving elevons were not realized to keep the research platform as simple as possible [1]. The COG is left at the recommended spot from the stock version. To increase the available space below the canopy, the rudder and elevator servo were moved back behind the wings.

Figure 3.2: The left picture shows the elevator with the maximum deflection of approx. 50°. The right one shows the neutral position.

3.3 Sensors and Flight Controller

As flight controller, a Pixhawk 1 running PX4 is used. This combination provides a large scope of possible code modifications and a reliable data logging. The PX4 software has been adapted to make automatic deep-stall maneuvres possible. It is supported by several different external sensors. The airspeed is measured by a pitot-tube and a differential pressure sensor. The mount of the pitot-tube is on the wing to reduce the influence of the propeller to a minimum. Additionally, and ADIS 16488 with a triaxial gyroscope, triaxial digital accelerometer, triaxial digital magnetometer, digital pressure sensor and a temperature sensor is used. It is mounted on top of the fuselage to reduce the influence of the high current wires and the vibrations of the motor. However, the Pixhawk onboard sensors can be used as well. To determine the position, an external GPS antenna is attached to the canopy. To get even more exact information, two vanes are added, one on each

wing. They are mounted far enough from the fuselage to minimize the propeller influence. Turning into the wind lies in the nature of a vane. Therefore, they allow to measure the airflow angle with reference to the airplane. The vanes are read with an Hall-sensor. (Figure: 3.3) The signals of the vanes and the airspeed sensor are transmitted by an I2C signal. A LIDAR-Lite determines the distance to the ground.

Three satellite receivers mounted perpendicularly to each other, ensure a stable connection between transmitter and receiver at any time and at any attitude. A telemetry module is used to maintain the connection with the ground station. Due to its limited bandwidth and to provide a higher resolution, the data gets logged on an SD-card.

To visualize the airflow over the wing, several yarn threads are attached on the wing and a small camera is mounted on the right wing tip. Furthermore, the drag of this camera is used to oppose the motor inertia and slipstream effect.

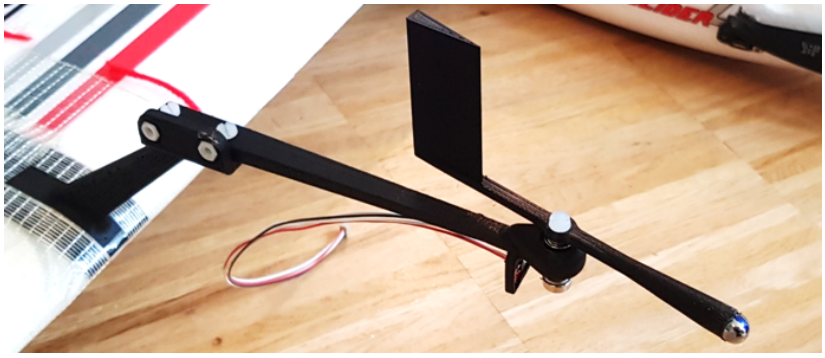

Figure 3.3: This picture shows the slip vane. It is balanced to reduce the influence of gravity.

3.4 Calibration

3.4.1 Airspeed Sensor and Vane Calibration

Several sensors need to be calibrated to obtain reliable data. First, the pitot tube is calibrated. This is necessary since slight mounting offsets, different tube lengths and similar uncertainties lead to wrong readings. The calibration is done by circling at constant speed, bank, radius and altitude for a few rounds. The gathered airspeed values can be compared with the GPS values. By doing a least square analysis, the airspeed scale factor can be determined and used for further flights.

To calibrate the vanes, two steps are needed. First, the Hall-sensor is calibrated while on the ground by using a template. The angle of attack vane is calibrated from -50° up to 70°. The slip vane gets calibrated from -40° to +40°. The aforementioned asymmetry allows accounting for the optimal Hall-sensor precision since there are much higher positive angles of attack expected than negative ones or slip angles. In a second step, the mounting error needs calibration. Several figure eights are flown at a day with no vertical wind and low speed horizontal wind. They are flown at constant altitude, speed and at the lowest bank possible. A least square analysis leads to the mounting offset, by reconstructing the inertial flow velocity using the vanes, airspeed measurements and wind estimates and comparing them to the inertial GPS velocity.

3.4.2 Elevator Deflection

The PX4 flight controller software logs servo outputs in PWM signals. Thus, we don't know the elevator deflection. However, a mapping function for the elevator deflection to PWM value is obtained by fitting a curve through the corresponding values. Equation 3.1 contains the formula used to convert the PWM values to degrees. Be aware that the lowest elevator PWM value corresponds to the highest elevator deflection.

$$e_{deg} = e_a * e_{PWM}^2 + e_b * e_{PWM} + e_c \tag{3.1}$$

Table 3.1: The fitting parameters used for the PWM to elevator deflection conversion.

Parameter	Unit	Value	Meaning
e_a	°	-4.864e-5	Fitting parameter of elevator conversion
e_b	°	0.0719	Fitting parameter of elevator conversion
e_c	°	28.253	Fitting parameter of elevator conversion
e_{PWM}	PWM		Elevator deflection as PWM signal

3.5 Pitot Tube at different angles of attack

For a better understanding of the reading of a pitot-tube at different angle of attacks and airspeeds, wind tunnel tests have been performed. A specially designed mount (Figure 3.4) is used to keep the ports of the tube in the center of the tunnel at the desired angle. Angles from -15° up to 45° have been covered. Lower negative angles of attack are not expected and after a 45° angle of attack, no airspeed can be measured. Data is gathered for wind speeds from $5\frac{m}{s}$ up to $13\frac{m}{s}$. The following measurement procedure is performed. The desired angle gets set and the wind speed is measured with an anemometer. After a while, the speed gets changed and measured again. This is repeated for several speeds and angles. Figure 3.5 shows the measured airspeed against different angles of attack. Each line represents one wind speed setting. There is an interesting effect to mention. The dip at 0° is caused by the geometry of the tube and can be observed by similar tubes as well [22]. The circles are the measurements whereas the lines are the corresponding fits. Fitting the data with a cosine did not lead to the expected results. Therefore a third order polynomial function for the region from -15° up to 40° is chosen. It is important to note, that this function does not account for symmetry and covers only the aforementioned bandwidth. However, it is valid to neglect lower angles of attack values, since they are not encountered during deep-stall maneuvers. The same parameters are used for all speed set points. This allows to use one function over the whole airspeed range. The disadvantage of this approach are worse fits at high and low speeds. The chosen function is shown in equation 3.2. However, in this project the angles of attack where usually too high and thus, this function has not been used. Anyhow, it is still a useful tool for future projects at lower angle of attacks or for the use of several pitot-tubes.

$$v_{measured} = w_a * v_0 + w_b * aoa_{deg} + w_c * aoa_{deg}^2 + w_d * aoa_{deg}^3 \tag{3.2}$$

Table 3.2: The fitting parameters used to fit the measured airspeed drop at high angles of attack.

Parameter	Unit	Value	Meaning
w_a	°	1.036	Fitting parameter for airspeed and AoA relation
w_b	°	0.0188	Fitting parameter for airspeed and AoA relation
w_c	°	0.00124	Fitting parameter for airspeed and AoA relation
w_d	°	-9.804e-5	Fitting parameter for airspeed and AoA relation
$v_{measured}$	$\frac{m}{s}$		measured airspeed
v_0	$\frac{m}{s}$		measured airspeed at 0° angle of attack

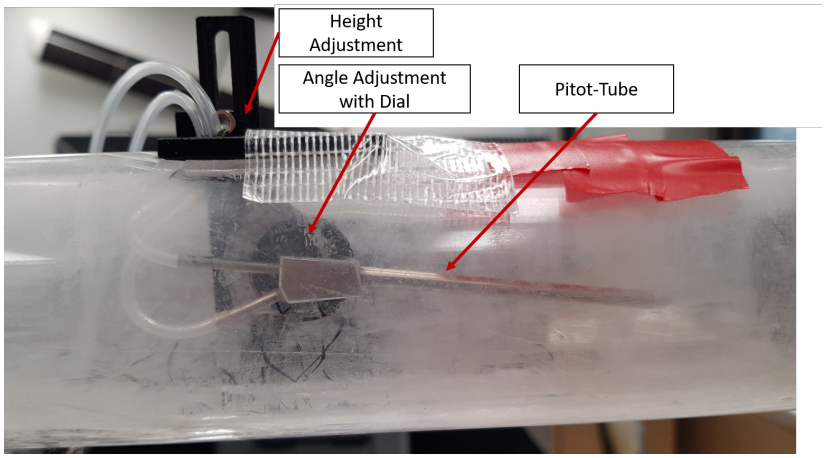

Figure 3.4: The mount allows to adjust the angle of the pitot-tube. To prevent boundary layer effects from the wind tunnel, the mount is height adjustable and keeps the ports in the middle of the tunnel.

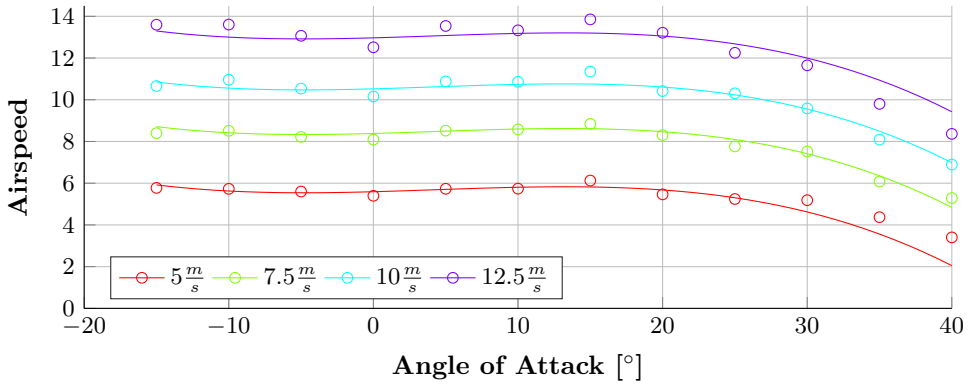

Figure 3.5: The measured airspeed is plotted against the angle of attack. Each color represents one wind speed setpoint. The legend values are the true airspeed values, i.e., the readings obtained from the anemometer.

Chapter 4

Experimental Procedures

4.1 Stall Entry

The stall entry is investigated manually first. To do so, the flight controller stabilizes the longitudinal axis using the ailerons. The elevator is controlled by the pilot. The plane gets slowed down and the elevator gets pulled back completely. This has to be done carefully to prevent a looping. As soon as the plane has slowed down enough it is pretty easy to fly the plane in deep-stall. The rudder can be used to turn, the motor and the elevator regulate the velocity and the sink rate. At certain elevator to thrust combinations, the rudder authority is too small and the plane turns uncontrolled.
In a second step this is implemented autonomously. Turning the plane into the wind gives the best results. The transition is more stable and the ground speed is slower. To achieve this, the PX4 wind estimate is used. There is no vertical wind component computed in the stock version and thus, just a 2D-wind estimate is used. However, the vanes could be used to compute a 3D-wind estimate.
As soon as the plane has finished said maneuvre, the wind estimate is frozen and the elevator is set to a defined value. This is usually the maximum deflection angle. To prevent a looping, a linear soft constraint is used which is triggered after a predefined critical angle. Additionally, a ramp is used to slow the elevator movement down.
After all, a looping is not something bad which has to be prevented at all cost. The plane is able to enter a deep-stall via a looping as well. Less altitude is needed and the whole maneuvre is easier to control without it.
The controller checks if the plane is stable for a certain time by observing if its attitude lays within reasonable boundaries.

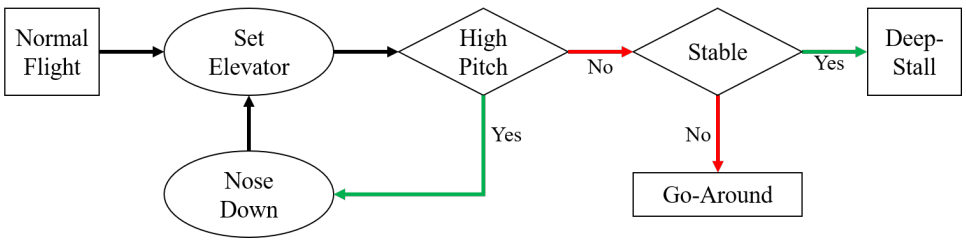

Figure 4.1: The transition process from normal flight to stable deep-stall is shown in this figure. Red arrows correspond to false statements and green arrows correspond to true ones.

4.2 Maintain Stall

As soon as the stability criterion is fulfilled, the controller proceeds with the maintain-stall procedure. The rudder keeps the plane pointing into the wind. The wind direction is assumed to be constant. In deep-stall, high angles of attack (up to 70°) are achieved. The airspeed sensor stops working under such extreme conditions (Section 3.5). This means, that no wind estimate is possible any more. The elevator and the motor are used to control the velocity. During the whole process, the controller checks if the plane is either too low, too fast or unstable. If one of those criteria is triggered, the controller switches back to normal flight mode and performs a go-around.

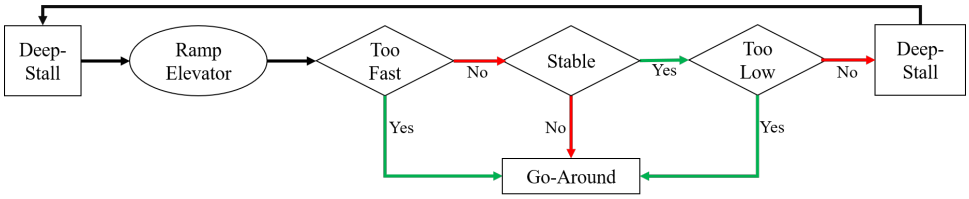

Figure 4.2: This figure shows the behaviour of the airplane while collecting data in the deep-stall state. Red arrows correspond to false statements and green arrows correspond to true ones.

4.3 Stall Landing

Safe deep-stall landings have been done manually. The plane is approaching in deep-stall at a low throttle setting. In the last few meters, the motor is used to reduce the sink rate below a feasible value. An autonomous deep-stall landing is not within the scope of this work. Besides said approach, a back transition to normal flight and a normal fixed wing landing can be considered (Figure 4.3). Such approaches would be best fitted for clearances with high obstacles around but with a smooth surface inside it. It would allow to land in a more careful manner without exposing fragile payload to high g-forces.

4.4 Data Collection

The aim of the data collection is to define a feasible space of elevator deflection and thrust. Additionally, the gathered data points are used to get a look up table or to fit a surface on the data which can be used to base a later precision controller on. The collected data is an essential step on the way to a precise deep-stall landing controller. To collect these data points in an efficient manner, the following procedure is used. The plane loiters to a predefined altitude (150m AGL). In a next step, the plane enters deep-stall. The thrust gets set to a fixed value which gets incremented after every stall loiter cycle to cover the whole thrust band. The elevator deflection gets slowly ramped (20 seconds) from the maximum to zero. Thus, we can assume steady state behavior. Repeating this cycle for several times covers a broad range of possible flight states. To reduce noise and outliers, this procedures has to be repeated several times. A termination criteria needs to be added to determine if the descent trajectory has been terminated due to too low altitude or something important like unstable flight states or too high airspeed. In both later cases, the metrics gets influenced.

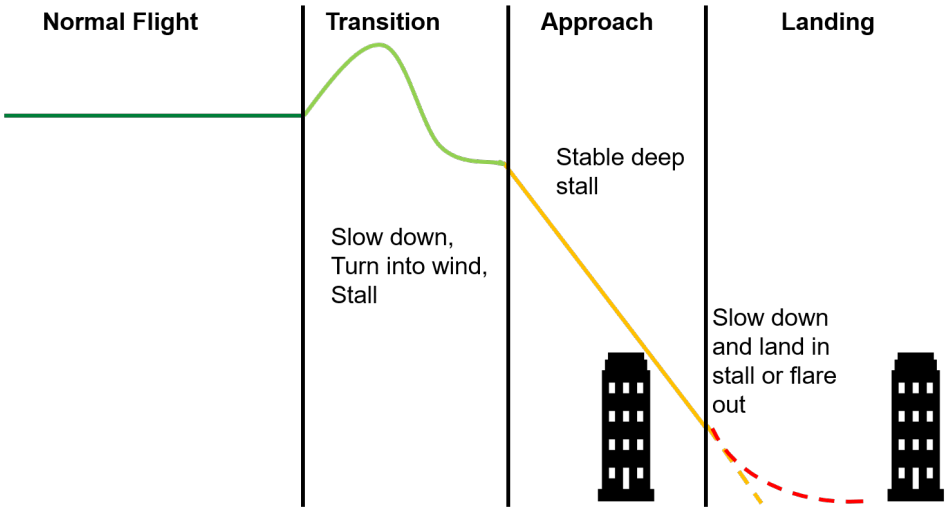

Figure 4.3: After the normal flight phase, the vehicle turns into wind, stalls and enters a stable deep-stall state. It can approach on a steep glide path between two obstacles and either land in a slowed down deep-stall or flare out if there is an appropriate surface.

4.4.1 Pre-Stall Data Collection

Pre-stall data has been collected to obtain a wider data set of data for an in-depth understanding over the whole width of possible angles of attack. Therefore, the lift and drag coefficients are determined for both regimes, the attached and the separated one. The maneuvre gets adapted. The plane flies leveled with no thrust. In a second step, the elevator ramps up slowly (60 seconds to reach the maximum deflection). As soon as the plane stalls, the data collection is stopped.

Chapter 5

Results and Analysis

Several single descent trajectories need to be measured to understand the effects of deep-stall on small UAVs with and without thrust. In this analysis up to 104 trajectories are considered. If not stated otherwise, thrust is plotted dimensionless from zero, which equals no thrust, to one which equals maximum thrust.

5.1 Vertical Speed

Figure 5.1 plots the sink rate against the thrust and the elevator deflection. The colored lines correspond each to one single descent trajectory. The sink rate values are not wind independent. It is not possible to estimate the wind during stall with the current development platform. However, the data collection was done at calm days. Each colored line represents a single descent trajectory. The whole dataset contains more than 100 of them. The descent rate seems to be linearly dependent on the thrust and elevator states. Thus, a linear plane (Equation: 5.1) has been fitted to describe the behavior. By investigating the range of the data, sink rates ranging from $1\frac{m}{s}$ up to $7\frac{m}{s}$ are possible. The descent rate is reduced either by increasing the thrust or by reducing the elevator deflection and vice versa. This shows that thrust has a major influence on the deep-stall behavior. However, as mentioned in the introduction, several theoretical and practical papers did not account for it.

$$V_v = a * t_{PWM} + b * e_{PWM} + c \tag{5.1}$$

Table 5.1: The fitting parameters of the linear plane describing the sink rate to thrust and elevator deflection ratio.

Parameter	**Unit**	**Value**	**Meaning**
a	$\frac{m}{s}$	-0.00339	Fitting parameter of sink rate plane
b	$\frac{m}{s}$	-0.00593	Fitting parameter of sink rate plane
c	$\frac{m}{s}$	16.93	Fitting parameter of sink rate plane
V_v	$\frac{m}{s}$		Sink rate
e_{PWM}	PWM		Elevator deflection as PWM signal
t_{PWM}	PWM		Thrust as PWM signal

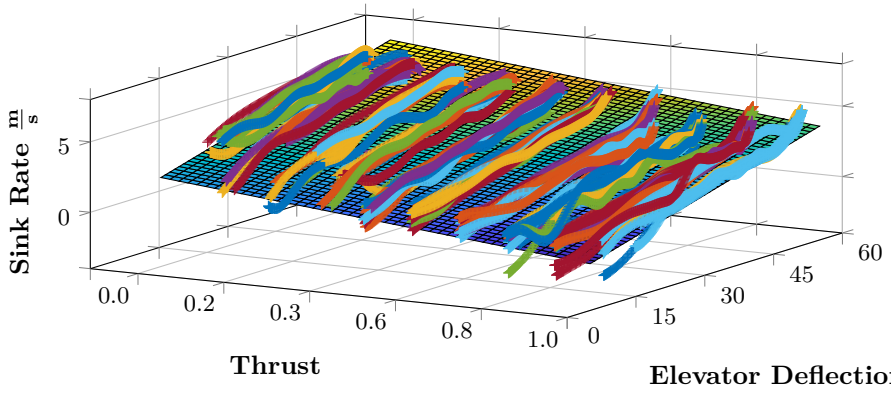

Figure 5.1: The sink rate is plotted versus thrust and elevator deflection. Each coloured line represents a single descent trajectory. In total, results from 104 descents were collected. A linear dependency can be seen and thus, a plane is fitted.

5.2 Horizontal Speed

Figure 5.2 plots the horizontal speed against the thrust and the elevator deflection. The solid lines show the average horizontal speed of the different descent trajectories at different thrust settings. The transparent part shows the corresponding variance. The horizontal speed is the measured horizontal GPS velocity minus the fixed horizontal wind estimate obtained from the PX4 wind estimator before starting the transition. With the used sensors, it is not possible to determine the wind in deep-stall, since there is no airspeed reading. The horizontal speed averages from $2.5\frac{m}{s}$ up to $5.5\frac{m}{s}$. Interestingly, the lowest speed is found at medium thrust settings. Most likely, caused by following effect. At higher thrust settings higher angles of attack are achieved. This leads to an increased drag. On the other hand, at high thrust settings, the increased drag doesn't suffice to counteract the additional thrust. Thus, at minimum and maximum thrust a similar horizontal speed of approximately $4\frac{m}{s}$ is observed. However, looking at the variance, high speed settings are less consistent than low ones. Mainly, due to the observed instabilities and an increased flow over the wing, which could lead noisier data.

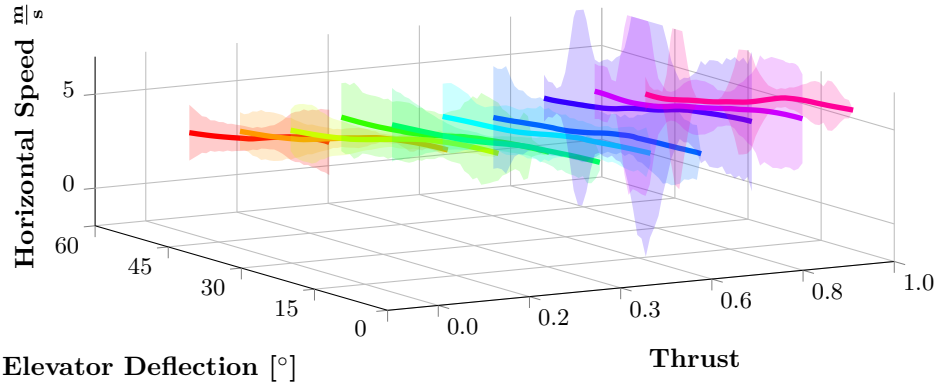

Figure 5.2: The average horizontal speed at each thrust setpoint is plotted against elevator deflection and thrust. Furthermore, the transparent area shows the variance at the corresponding spot.

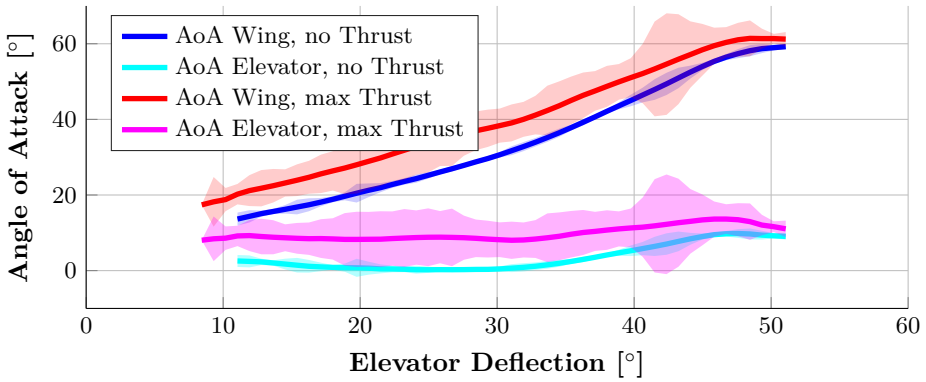

Figure 5.3: The angle of attack is plotted versus the elevator deflection. The blue and the red line show the angle of attack of the main wing. The magenta and cyan line show the angle of attack of the elevator. The red and the magenta line show the results for maximum thrust whereas the cyan and the blue one represent no thrust.

5.3 Angle of Attack

Figure 5.3 plots the angle of attack of the wing and the elevator against the elevator deflection. The angle of attack is measured using the corresponding and calibrated vane. To improve the readability, just the data for maximum thrust and zero thrust is shown. Additionally, the different descent trajectories at the said thrust settings are binned. Thus only one curve and one variance is shown for each state. The upper two curves show the angle of attack of the main wing. As more thrust is applied, ever higher angle of attacks can be achieved. In this case angles up to 65° were observable. On the other hand, the variance increases massively. Indicating that those states are much less stable than the zero thrust states. Considering the results from section 3.5 it is not possible to get an airspeed reading above 45°. This corresponds well with the observations made during the deep-stall data collection. The two lower lines represent the angle of attack of the elevator. It can be seen that it stays at a much lower angle of attack and thus an attached flow can be maintained. However, especially at high thrust, the elevator gets close to critical angles of attack. Besides that, the main observations from the main wing can be applied to the elevator as well.

5.4 Lift and Drag

Figure 5.4 shows the pre-stall and post-stall data for the C_L values. They have been computed using the formulae from section 2.3. The used airspeed is the difference of horizontal GPS velocity and the fixed wind estimate in the horizontal plane. The vertical speed component is just the vertical GPS speed. Again, the data collection was performed on calm days. Using the conventional linear approach from equation 2.7 for the pre-stall regime gives the dashed cyan line. The data in the post-stall regime gets fitted using an extended flat plate approach. The equation from 2.5 gets extended to:

$$C_L = k_{flat} sin(2 * \alpha + \alpha_{shift}) \tag{5.2}$$

This allows to account for shifting and scaling and thus to get a better fitting while seeing how well the flat plate theory is applicable to the used airframe. The magenta dashed line is obtained. α_{shift} gets calculated from C_{L_0} this allows to have both

curves crossing the x-axis at the same point and thus basing on the same C_{L_0} . By freezing the parameters of both functions, it is now possible to use the distribution function from equation 2.9 fitting both functions into one and still accounting for the two states separately. In the transition phase, there is no data available since steady state measurements are not possible there without the use of a wind tunnel. Mostly, because a plane in this flight phase is inherently unstable. The flat plate approach works surprisingly well. However, it is necessary to scale and shift it. The shift corresponds to the pre-stall data. Due to the cambered airfoil, the intersection of the x-axis and the pre-stall curve lays at a negative angle of attack. The scaling can be explained by the use of an airplane instead of an infinite flat plate.

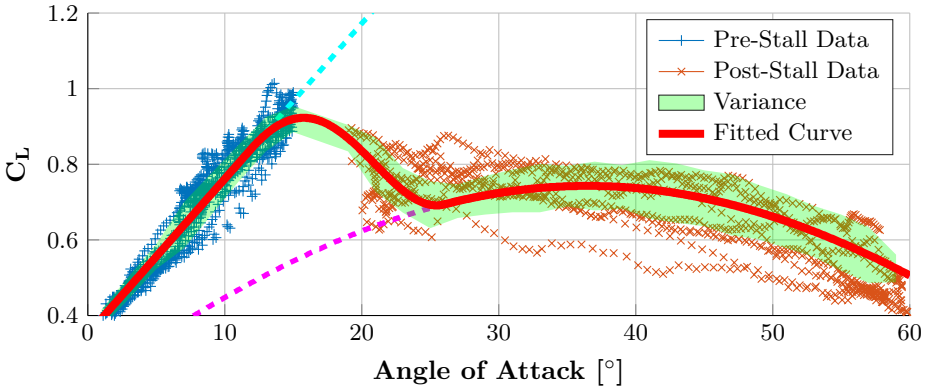

Figure 5.4: The blue pluses represent the measured pre-stall lift coefficients, the orange crosses show the measured post-stall lift coefficients. The attached flow behaviour is modelled using a linear approach (Cyan dashed line). An extended flat plate approach fits the behaviour in the separated flow region (Magenta dashed line). A sigmoid like distribution function is used to combine both approaches (Red line). The transparent green area represents the variance for a bin width of 2°.

In figure 5.5 a similar approach has been used to fit the drag coefficients. The C_D values are computed similar to the C_L values. The data in the attached flow region are fitted using the equation 2.8. The cyan dashed line represents it. Fitting the values in the post-stall region is done by using the extended flat plate equation and shown as the dashed magenta line. The same parameters for the distribution function are used as for the distribution function of the C_L fitting. Therefore, both curves can be compared better and used for further calculations like the airplane efficiency. However, fitting each parameter (C_L and C_D) for itself could lead to more exact fittings.

$$\begin{aligned} C_D =& C_{D_{min}} + (C_{D_{max}} - C_{D_{min}}) sin(\alpha)^2 \\ &\text{With } C_{D_{min}} > C_{D_0} \end{aligned} \tag{5.3}$$

This allows for scaling and shifting. The same distribution function obtained for C_L is used to combine both models. Table 5.2 lists the used parameter and their values.

Figure 5.6 shows the airplane efficiency. It is obtained by dividing the two fitted functions for C_L and C_D and plotting the result against the angle of attack. It shows, that the airplane efficiency at high angle of attack is much lower than at low ones. This was expected and it plays a crucial role in deep-stall approaches, which allows a massively increased drag with reduced lift. The aforementioned is essential for steep approach angles at low speed.

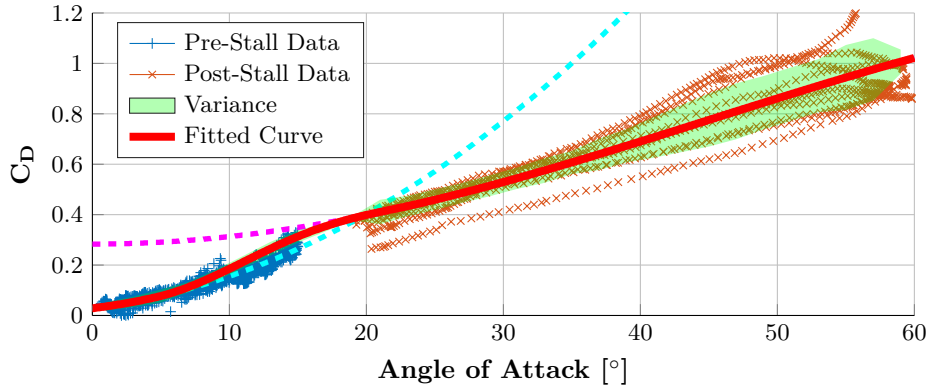

Figure 5.5: The blue pluses represent the measured pre-stall drag coefficients, the orange crosses show the measured post-stall drag coefficients. The attached flow behaviour is modelled using equation 2.8.(Cyan dashed line) Using an extended flat plate approach fits the behaviour in the separated flow region. (Magenta dashed line). A sigmoid like distribution function is used to combine both approaches (Red line). The transparent green area represents the variance for a bin width of 2°.

Table 5.2: Different parameters used to fit the C_L and C_D curves.

Parameter	**Unit**	**Value**	**Meaning**
C_{L_0}	[]	0.356	C_L at 0° angle of attack
C_{L_α}	[]	2.354	Slope of the C_L fit for α in radians
k_{flat}	[]	0.7428	Scaling factor
α_{shift}	Deg	17.06	Shifting of flat plate approach. Computed from C_{L_0}
C_{D_0}	[]	0.0288	C_D at 0° angle of attack
C_{D_α}	[]	0.3787	Linear fitting coefficient
$C_{D_{\alpha_2}}$	[]	1.984	Quadratic fitting coefficient
$C_{D_{min}}$	[]	0.2832	Minimally reachable C_D
$C_{D_{max}}$	[]	1.268	Maximally reachable C_D
α_{cut}	rad	0.3312	Angle at which the regions change
$\Delta\alpha$	rad	0.2453	Width of the transition region

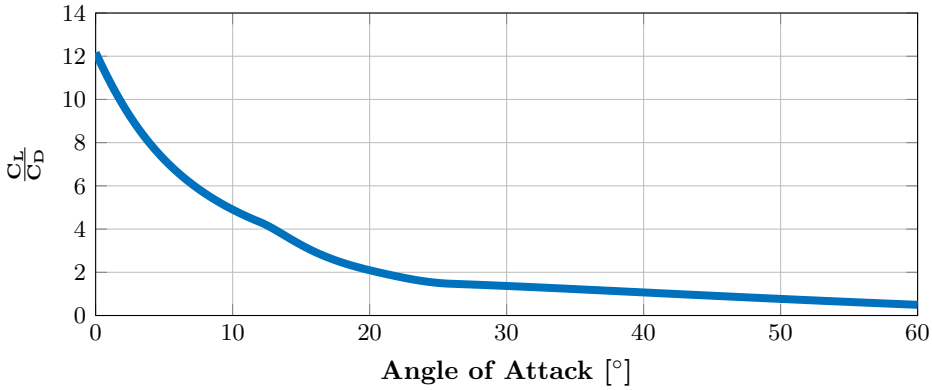

Figure 5.6: This figure shows the $\frac{C_L}{C_D}$ values against the angle of attack. This represents the airplane efficiency.

In figure 5.7 the inertial vertical force distribution against the flightpath angle is shown. There are two point clouds. The one maxing at high absolute flightpath angles is representing drag whereas the other-one represents lift. The lines are the combination of both values and represent the total vertical force. It explains what keeps the plane airborne considering there is barely any velocity and attached flow. At high flightpath angles, the vertical component of the drag outperforms the vertical component of the lift by far and thus, the plane stays airborn thanks to drag.

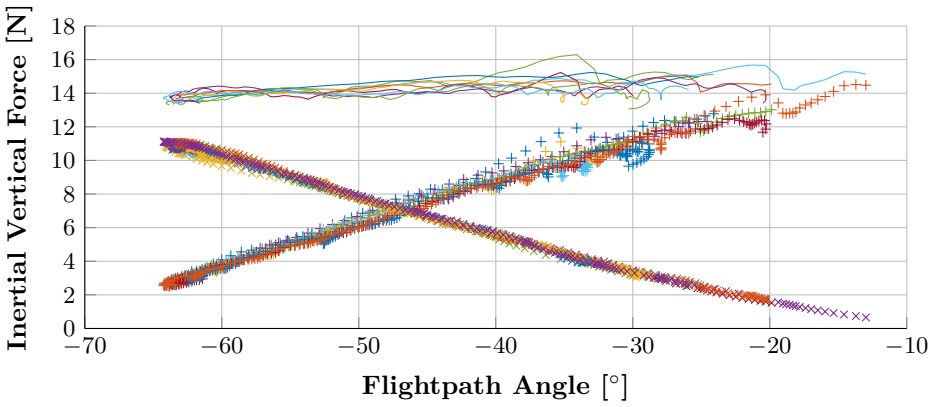

Figure 5.7: The inertial vertical force is plotted against the flightpath angle. The data cloud descending from the upper left corner to the bottom right represents the vertical component of the drag. The other cloud ascending from the bottom left to the top right represents the vertical lift components. The lines are a combination of both values.

5.5 Utility Function

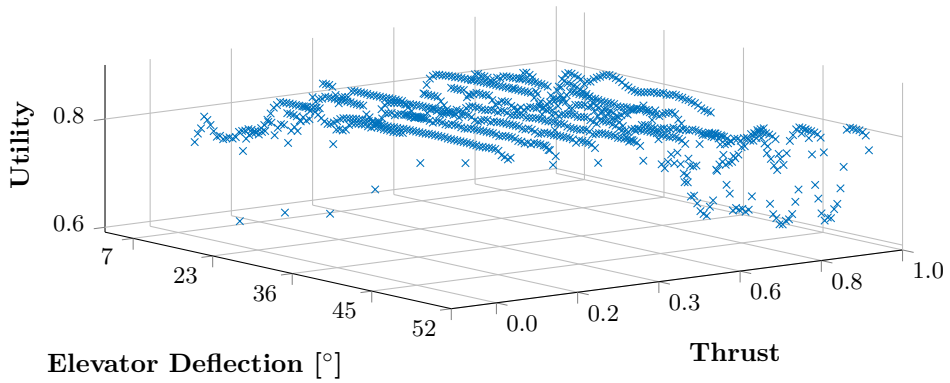

Figure 5.8: The utility values are distributed over the whole range of input parameters. They are initialized as one and reduced by the applied penalty.

A utility function has been derived from the collected data to obtain an optimal base for future controller. A metric has to be introduced. This allows to derive a function which is used to find the optimal elevator and thrust setpoint for a wished control variable. Since the derived function is an utility function, the optimal setpoint combination is always found at the optimum of this function.

Control Penalty

It is essential to reduce the power consumption to a minimum especially during the early phase of the approach. This allows for landing with less battery reserves, which directly correspond to an increased range. A linear penalty reciprocally proportional to the thrust level is introduced to consider this in the utility function. The thrust penalty is formulated in equation 5.4.

$$P_{Thrust} = \frac{Thr}{Thr_{max}} \tag{5.4}$$

Stability

The plane needs to be stable during the whole maneuvre. A unstable flight state leads to a go-around and to either a new transition maneuvre or a complete abortion of the landing attempt. Depending on the surroundings, this may not be possible and could lead to a crash. There are several reasons which could explain the instability. The most common ones are the transitions back to the normal flight state if the plane gets too fast or if the plane enters a left spin caused by a lack of control authority. The termination criterion is used to detect complete instability. A penalty gets applied on all elevator deflections with the same thrust level which are less than the one which triggered the criterion. The termination criterion triggers the penalty if the descent was terminated because the plane was too fast or unstable. (Equation: 5.5) Additionally, the yaw and sink rate variance are considered as well as an indicator for stability. (Equation: 5.6 and 5.7)

$$P_{Termination} = (2)(1 - 1 * 0.5^n)$$
With n being the amount of times the termination criterion has been triggered at higher elevator deflection with the same thrust setpoint. (5.5)

$$P_{v_{yaw}} = \frac{tanh(var(r_{yaw}))}{\frac{\pi}{2}} \tag{5.6}$$

$$P_{v_{sink}} = \frac{tanh(var(v_{sink}))}{\frac{\pi}{2}} \tag{5.7}$$

$$P_{Stability} = P_{v_{sink}} + P_{v_{yaw}} + P_{termination} \tag{5.8}$$

Control Authority

The control authority has to be guaranteed at all time. Otherwise, the plane gets unstable or can't be kept on the desired trajectory. A major loss of rudder authority is observable at high elevator deflections and thrust levels. This swerve to the left is caused by asymmetric thrust at high angle of attack, torque, gyroscopic precision and the slip stream effect. To counteract this issue, a penalty is introduced which gets triggered if the yaw acceleration acts in the other direction than the rudder (Equation 5.9). The yaw acceleration is obtained by deriving the yaw rate.

Further, a penalty is introduced for areas close to the borders of possible input parameters. This prevents being pushed into a corner where the controller is limited in its actions. (Equation 5.10)

$$P_{yawaut} = \frac{tanh(constrain(a_{yaw} * p_{rudder}, -inf, 0))}{\frac{\pi}{2}} \tag{5.9}$$

$$P_{border} = (\frac{1}{(i_e)^2} + \frac{1}{k_b * (i_{e_{max}} - i_e)^2} + \frac{1}{i_t^2} * \frac{2i_{t_{max}}}{i_e} + \frac{1}{(i_{t_{max}} - i_t)^2} * \frac{i_{t_{max}}}{i_{e_{max}}}) \tag{5.10}$$

$$P_{ConAt} = P_{border} + P_{yawaut} \tag{5.11}$$

$$P_{tot} = \lambda_{weights} * [P_{Thrust}, P_{termination}, P_{yawaut}, P_{v_{yaw}}, P_{v_{sink}}, P_{border}]^T \tag{5.12}$$

Table 5.3: A list of the parameters used to calculate the metrics.

Parameter	**Meaning**
P_{tot}	Total penalty
P_{Thrust}	Thrust penalty
$P_{Stability}$	Instability Penalty
P_{ConAt}	Control authority penalty
P_{border}	Close to border penalty
P_{yawaut}	Rudder authority penalty
P_{vsink}	Sink rate variance penalty
P_{vyaw}	Yaw rate variance penalty
$P_{Termination}$	Termination penalty
Thr	Thrust
Thr_{max}	Maximum Thrust
r_{yaw}	Yaw rate
v_{sink}	Sink rate
p_{rudder}	Rudder Position in centred PWM
a_{yaw}	Yaw acceleration
i_e	Elevator index of bin
$i_{e_{max}}$	Number of elevator bins
i_t	Thrust index of bin
$i_{t_{max}}$	Number of thrust bins
k_b	Parameter to flatten penalty

A 10 by 100 bin mesh gets initialized covering all input states. All bins have a utility value of one in the beginning. After that, the metrics get applied and computed for each bin. The different penalties are weighted differently with the penalty-vector $\lambda_{Weights}$ (Equation: 5.13). The values are chosen to account for different characteristics and importance of the different penalties.

$$\lambda_{Weights} = [0.755, 1, 3, 2, 10, 1.5] \tag{5.13}$$

Figure 5.8 shows the values of the different bins after the total penalty (Equation 5.12) has been applied. There are two interesting regions. At low thrust and low deflection, maintaining deep-stall is not possible because the plane gets too fast and starts flying again. The other interesting region is found at high thrust and high elevator deflection. There, the plane swerves to the left (Section: 2.4) and the rudder authority is lost. There are several options to handle this issue, like increasing the rudder size, adding elevons, improving the yaw controller or using a twin engine tractor configuration.
In a second step, a fifth, forth order polynomial surface is fitted on the bin values. Bins below the fit threshold T_{fit} are weighted with factor $F_{fit_{Weights}}$. This ensures

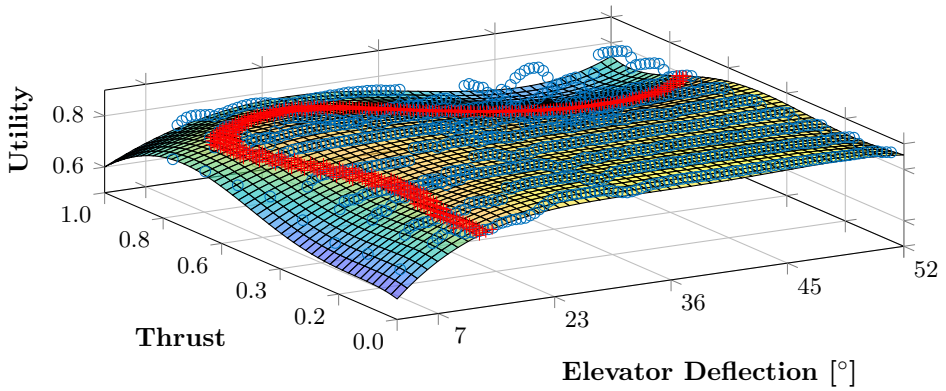

Figure 5.9: A fifth order polynomial function is used to fit the utility values. A threshold (red) can be applied to define the feasible space.

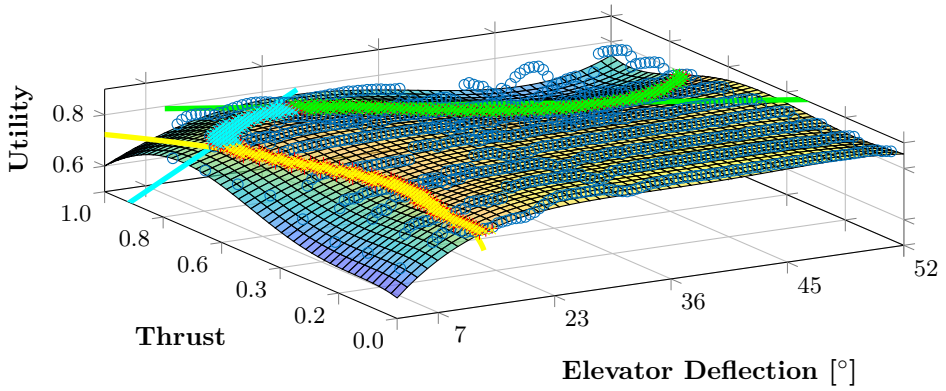

Figure 5.10: This utility function is too complicated. It has to be simplified. This is achieved by cropping it using two linear (cyan and green) and one quadratic (yellow) function.

that the fit accounts for the depressions with higher priority. Otherwise it can happen that the fit ignores crucial regions. Defining a threshold allows to mark the feasible space of input parameters. (5.9) Obviously, this function can't be used for a controller. It is computationally too expensive and there are several local maxima possible. As in figure 5.10 shown, two linear and a quadratic function are used to crop the surface at the defined threshold. (Equation: 5.14-5.16)
A second order polynomial surface is fitted after cropping out the feasible areas (5.11). A bin is considered feasible if condition 5.17 is fulfilled. The second order polynomial surface and the three border functions provide an easy to use and computationally cheap utility function. (Equation: 5.18)

$$e_{PWM_{c1}} = c_{a1} * t_{PWM} + c_{b1} \tag{5.14}$$

$$e_{PWM_{c2}} = c_{a2} * t_{PWM} + c_{b2} \tag{5.15}$$

$$e_{PWM_{c3}} = c_{a3} * t_{PWM}^2 + c_{b1} * t_{PWM} + c_{c1} \tag{5.16}$$

$$\begin{aligned} &e_{PWM_{bin}} < e_{PWM_{c1}}(t_{PWM_{bin}}) \\ \text{and } &e_{PWM_{bin}} > e_{PWM_{c2}}(t_{PWM_{bin}}) \\ \text{and } &e_{PWM_{bin}} > e_{PWM_{c3}}(t_{PWM_{bin}}) \end{aligned} \tag{5.17}$$

$$Utility = d + f*t_{PWM} + g*e_{PWM} + h*t_{PWM}^2 + k*t_{PWM}*e_{PWM} + l*e_{PWM}^2 \tag{5.18}$$

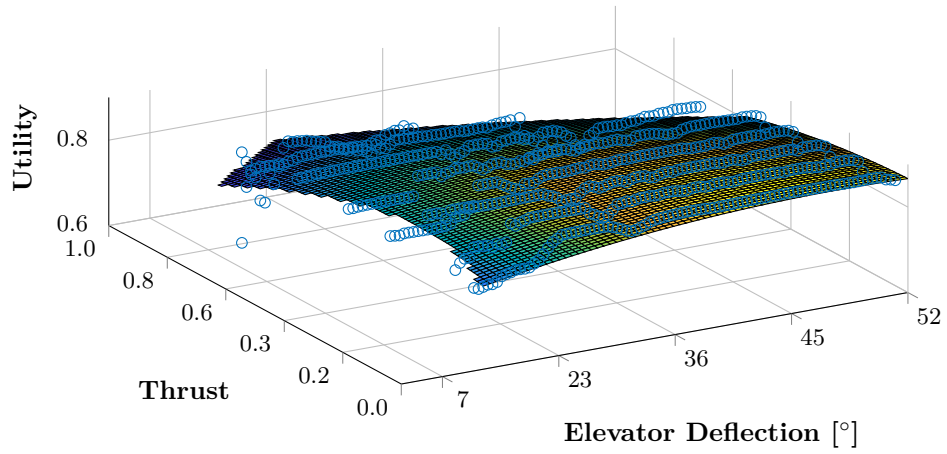

Figure 5.11: After the complicated utility function has been cropped and the excess bins have been removed, a second order polynomial function is fitted.

Table 5.4: The used fitting parameters to obtain the utility function.

Parameter	Value	Meaning
c_{a1}	1.765	Fitting parameter of first cropping function
c_{b1}	-1.824e3	Fitting parameter of first cropping function
c_{a2}	-1.072	Fitting parameter of second cropping function
c_{b2}	3.641e3	Fitting parameter of second cropping function
c_{a3}	6.159e-4	Fitting parameter of third cropping function
c_{b3}	-1.645	Fitting parameter of third cropping function
c_{c3}	2.7438e3	Fitting parameter of third cropping function
d	0.6138	Fitting parameter of simplified utility function
f	1.627e-4	Fitting parameter of simplified utility function
g	3.017e-4	Fitting parameter of simplified utility function
h	-1.862e-7	Fitting parameter of simplified utility function
k	2.191e-7	Fitting parameter of simplified utility function
l	-2.435e-7	Fitting parameter of simplified utility function
$F_{fit_{Weights}}$	10	Factor to increase value of low bins
T_{fit}	0.75	Threshold defining low bins

5.6 Possible Control Approach

In the following few paragraphs a possible control approach is explained. The sink rate is used as an example. It is essential to control it before ground contact and allows to influence the flightpath angle as well. In a first step, a sink rate (v_{sink}) has to be determined. The intersection of the aforementioned and the fitted sink rate plane (Equation: 5.1) gives us a first order function (Equation: 5.19) of the possible thrust and elevator values (Figure: 5.12). Projecting this curve onto the utility function (Figure: 5.13) gives us a second order curve (Figure: 5.14, Equation: 5.20). This curve is depending on thrust and gives us a utility value in return. Deriving it and solving for zero gives the optimal thrust value for a given sink rate. Equation 5.22 allows to do the whole computation for a given sink rate in one step. The optimal elevator deflection is obtained by using the equation 5.19. In a last step, it has to be determined if the found parameter set lies within the feasible area. The three border functions are checked. If the point is outside of the feasible area, the closest intersection is chosen.

A curve showing all optimal values is obtained by calculating the optimal elevator deflection and the optimal thrust for the whole set of feasible sink rates. With this EasyGlider, sink rates from $1\frac{m}{s}$ to $7\frac{m}{s}$ are achievable. (Figure: 5.15)

$$e_{PWM} = -(a - v_{sink} + b * t_{PWM})/c \tag{5.19}$$

$$\begin{aligned} Utility = d + f * t_{PWM} + h * t_{PWM}^2 - & \frac{g * (a - v_{sink} + b * t_{PWM})}{c} \\ & + \frac{l * (a - v_{sink} + b * t_{PWM})^2}{c^2} \\ & - \frac{k * t_{PWM} * (a - v_{sink} + b * t_{PWM})}{c} \end{aligned} \tag{5.20}$$

$$\begin{aligned} \frac{\mathrm{d}Utility}{\mathrm{d}t_{PWM}} = f + 2 * h * t_{PWM} - & \frac{k * (a - v + b * t_{PWM}}{c} \\ & - \frac{b * g}{c} - \frac{b * k * t_{PWM}}{c} \\ & + \frac{2 * b * l * (a - v + b * t_{PWM})}{c^2} \end{aligned} \tag{5.21}$$

$$t_{PWM_{opt}} = \frac{2 * b * l(v_{sink} - a) + c * k * (a - v_{sink}) + b * c * g + c^2 * (-f)}{2 * (b^2 * l - b * c * k + c^2 * h)} \tag{5.22}$$

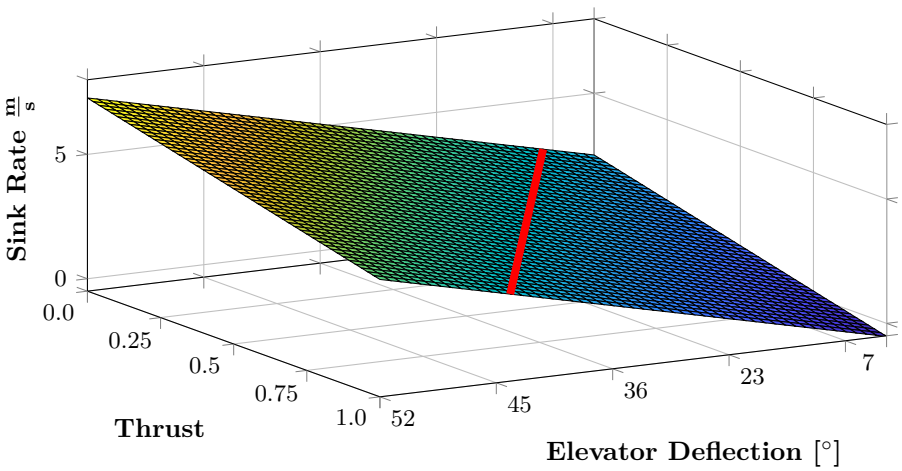

Figure 5.12: A linear curve is obtained by intersecting a given sink rate with the plane from figure 5.1.

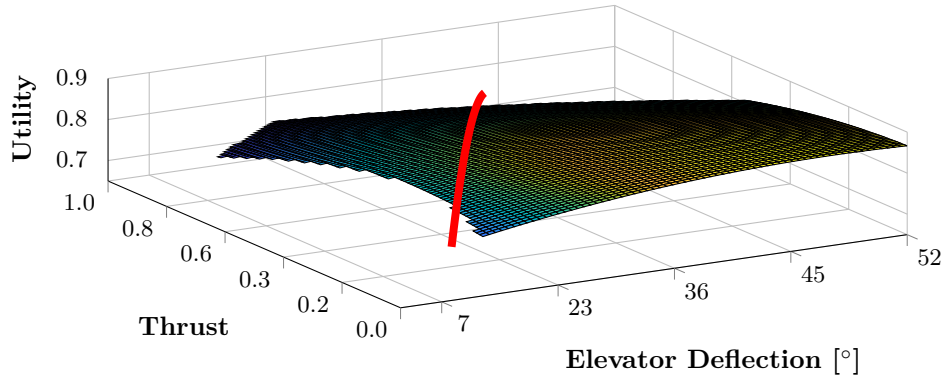

Figure 5.13: A quadratic curve is obtained by projecting the linear curve from figure 5.12 on the surface of the simplified utility function. (5.11)

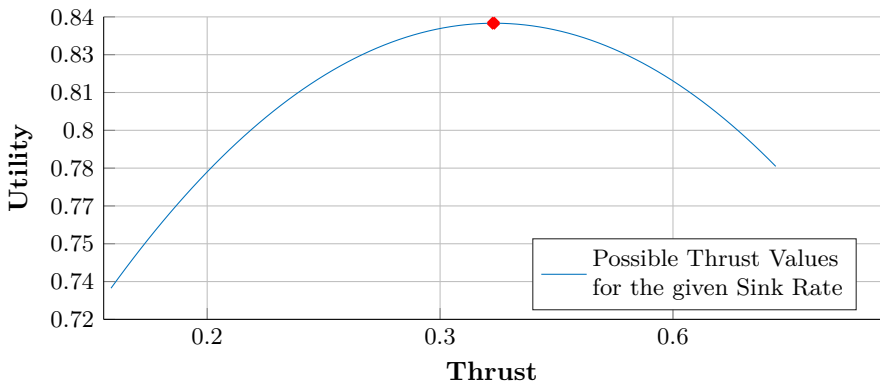

Figure 5.14: Extracting the function from figure 5.13 and projecting it onto the thrust utility plane gives the shown function. The optimal thrust level can be determined. (Red dot)

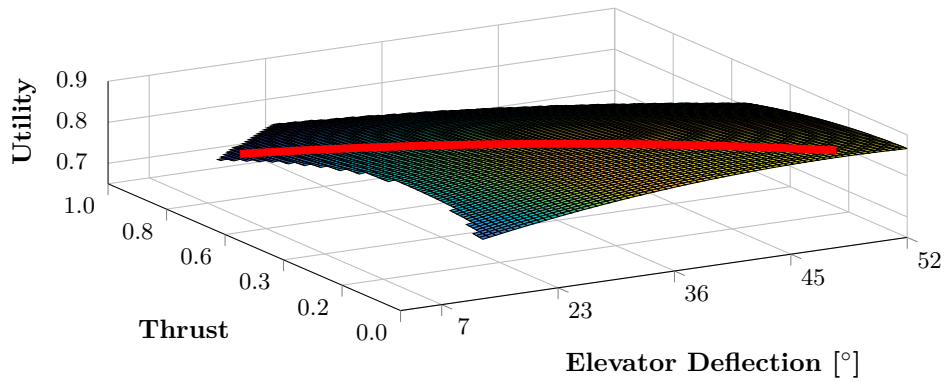

Figure 5.15: The red line shows the optimal states for a sink rate range from $1\frac{m}{s}$ to $7\frac{m}{s}$.

Chapter 6

Conclusion

In this work, the capability to enter deep-stall is shown for an EasyGlider with an all moving tail. The EasyGlider maintains deep-stall reliably and deep-stall landings are possible. Entering and maintaining deep-stall automatically is possible. This is achieved by a modified branch of the PX4 software. The derived utility function covers a wide set of input parameters. It defines a feasible state and helps to find the optimal controller feed forward signal for a given sink rate. Thus, it can be used by future projects to implement a high precision controller. A controller that allows to land at a predefined spot. It could be shown that the sink rate can be regulated using the elevator deflection and the thrust setting. Especially the effects of the thrust on the vertical and horizontal speed are worth mentioning. Increasing the thrust is reducing the sink rate. However, it is not necessarily increasing the horizontal speed. On the contrary, at low initial speeds, the horizontal speeds get reduced even further.
However, there are still some open questions which would be interesting to address in the future.

- Increase the feasible space by reducing the effects leading to a swerve to the left tendency by enlarging the rudder size, using elevons, implementing a more advanced yaw controller or by using a twin engine tractor configuration.
- Use a twin engine tractor configuration to investigate the influence of the prop wash on the wings and thus on the sink rate or the angle of attack, respectively.
- Investigate the influence of different aspect ratios on the deep-stall behavior. This would explain, whether a soaring plane or an acrobatic plane with the same wing area would have a better deep-stall approach and landing behaviour.
- To further increase the approach angle, the possibilities of a descending helix in deep-stall should be investigated. Theoretically, a large enough rudder and aileron authority should allow this.

Bibliography

[1] P. R. Thomas, S. Bullock, U. Bhandari, and T. S. Richardson, "Fixed-wing approach techniques for complex environments," *Aeronautical Journal*, vol. 119, no. 1218, pp. 999–1016, 2015.

[2] Z. He, Y. Y. Kan, and D. Li, *Deep Stall Landing Strategy for Small Fixed-Wing Aircraft Aided by Morphing*, ser. Chinese Control and Decision Conference. New York: Ieee, 2017, pp. 6772–6776.

[3] B. Cheng and Z. Guo, "Study on small uavs' deep stall landing procedure," in *2017 5th International Conference on Mechanical, Automotive and Materials Engineering (CMAME)*, Conference Proceedings, pp. 269–274.

[4] W. Crowther and K. Prassas, "Post stall landing for field retrieval of uavs," in *14th Bristol International unmanned air vehicle systems conference, UK*, Conference Proceedings.

[5] S. H. Mathisen, T. I. Fossen, T. A. Johansen, and Ieee, *Non-linear Model Predictive Control for Guidance of a Fixed-Wing UAV in Precision Deep Stall Landing*, ser. International Conference on Unmanned Aircraft Systems. New York: Ieee, 2015, pp. 356–365.

[6] H. Taniguchi, "Analysis of deepstall landing for uav," in *Proceedings of 26th International Congress of the Aeronatical Sciences*, Conference Proceedings.

[7] A. Waldock, C. Greatwood, F. Salama, and T. Richardson, "Learning to perform a perched landing on the ground using deep reinforcement learning," *Journal of Intelligent and Robotic Systems*, vol. 92, no. 3-4, pp. 685–704, 2018.

[8] J. Gundlach, *Designing unmanned aircraft systems : a comprehensive approach*. Reston, Va: Reston, Va. : American Institute of Aeronautics and Astronautics, 2012.

[9] "The last victor," https://web.archive.org/web/20120322161536/http://www.thevictorassociation.org.uk/?p=491, Last visited: 07.07.2019.

[10] P. J. Swatton, *The principles of flight for pilots*. Chichester, West Sussex, U.K: Chichester, West Sussex, U.K. : Wiley, 2011.

[11] L. LINA and M. MOUL, "A simulator study of t-tail aircraft in deep stall conditions," in *Aircraft Design and Technology Meeting*, Conference Proceedings, p. 781.

[12] G. Cooper and M. White, "Simulator studies of the deep stall," 1965.

[13] R. T. Taylor and E. J. Ray, "Deep-stall aerodynamic characteristics of t-tail aircraft," 1965.

[14] A. SIM, "Flight characteristics of a manned, low-speed, controlled deep stallvehicle," in *11th Atmospheric Flight Mechanics Conference*, Conference Proceedings, p. 2074.

[15] W. Blanchard Jr, "A flight investigation of the ultra-deep-stall descent and spin recovery characteristics of a 1/6 scale radiocontrolled model of the piper pa38 tomahawk," 1981.

[16] J. Wildi, 2019.

[17] N. Hall, "Drag equation," https://www.grc.nasa.gov/www/k-12/airplane/drageq.html, Last visted: 07.07.2019.

[18] W. Pointer, G. Kotsis, P. Langthaler, M. Naderhirn, and Ieee, *Using Formal Methods to Verify Safe Deep Stall Landing of a MAV*, ser. 2011 Ieee/Aiaa 30th Digital Avionics Systems Conference. New York: Ieee, 2011.

[19] J. Tangler and D. Kocurek, *Wind Turbine Post-Stall Airfoil Performance Characteristics Guidelines for Blade-Element Momentum Methods.*

[20] G. D. McBain, *Theory of lift : introductory computational aerodynamics in MATLAB/Octave.* Chichester: Chichester : Wiley, 2012.

[21] "Left turning tendencies," http://users.skynet.be/sky92472/Ltt.htm, Last visited: 07.07.2019.

[22] "Pitot-static - properties and characteristics," http://76.12.33.167/pitot-properties.html, Last visited: 16.07.2019.